Unified Understanding of Water Transport in Graphene Oxide–Modified Membranes: An Experimental and Molecular-Scale Perspective

Yan A. S. da Campo,[†] Ezequiel Lorenzett,[‡] Paulo A. Netz,[‡] Marcelo L. Pereira Junior,[¶,§] Claudia K. B. de Vasconcelos,[‖] Glaura G. Silva,[‖] Marcia C. Barbosa,[*,⊥] and Mateus H. Köhler[*,†]

†*Departamento de Física, Universidade Federal de Santa Maria, 97105-900 Santa Maria, Brazil*

‡*Instituto de Química, Universidade Federal do Rio Grande do Sul, 91501-970 Porto Alegre, Brazil*

¶*University of Brasília, College of Technology, Department of Electrical Engineering, 70910-900, Brasília, Federal District, Brazil.*

§*Department of Materials Science and NanoEngineering, Rice University, 77005, Houston, Texas, United States.*

‖*CTNano - Centro de Tecnologia em Nanomateriais e Grafeno, Departamento de Química, Universidade Federal de Minas Gerais, Belo Horizonte, Brazil*

⊥*Instituto de Física, Universidade Federal do Rio Grande do Sul, 91501-970 Porto Alegre, Brazil*

E-mail: marcia.barbosa@ufrgs.br; mateus.kohler@ufsm.br

Abstract

Understanding the mechanisms governing water transport in graphene oxide (GO)

membranes remains a central challenge in the development of next-generation desalination materials. In this work, commercial polyamide reverse osmosis membranes were coated with GO using an in situ dynamic pressurization method, followed by a comprehensive characterization and performance evaluation. Experimentally, GO deposition altered surface morphology, reduced roughness, and increased hydraulic permeability by ∼25% while maintaining salt rejection above 90%. Raman spectroscopy confirmed the incorporation of GO, and AFM and SEM revealed smoothing of the ridge-and-valley structure characteristic of interfacially polymerized polyamide layers. To elucidate the molecular origins of these changes, we performed a systematic series of molecular dynamics (MD) simulations that isolate the effects of slit width, interlayer spacing, and commensurability in stacked GO galleries. The simulations demonstrate that enhanced permeability is linked to the formation of low-friction pathways, reduced hydrogen-bond structuring, and the emergence of preferential flow routes within GO nanochannels. High commensurability between adjacent slits increases dynamic coupling and suppresses bottlenecks, while geometric expansion of the channels accelerates water mobility without compromising ion exclusion. By integrating experimental observations with molecular-scale analysis, this study provides a unified mechanistic picture of water transport in GO-modified membranes. The synergy between surface smoothing, nanoscale alignment, and reduced interfacial friction explains the observed enhanced permeance and highlights how targeted control of GO morphology can be leveraged to optimize membrane performance. These findings establish a multiscale framework for the rational design of high-flux, high-selectivity desalination membranes based on graphene-derived materials.

Introduction

Water scarcity is one of the most significant challenges of our time.[1] To define whether there is water scarcity, one must consider the amount of freshwater available to meet a population's needs.[2] Currently, approximately half a billion people live with severe water scarcity on a

year-round basis. At the same time, half of the global population is affected by severe water shortages for at least one month per year.[2] On top of that, of the total water on Earth, only 0.3% is freshwater readily available for human use. The remaining 99.7% is composed of 97% seawater and 2.7% freshwater stored in inaccessible locations, such as glaciers and deep aquifers. Water scarcity is a growing problem, driven by factors such as intense industrial use and rapid population growth.[3] This situation underscores the urgent need to adopt sustainable measures for managing water resources.

Effective approaches to combating water scarcity include improving water conservation systems, promoting water reuse and recycling, and increasing water-use efficiency across all major consumption sectors.[4] In practice, however, a more direct and increasingly common solution has been desalinating seawater, which provides a long-term water supply to help mitigate scarcity.[5]

Of the various desalination processes, reverse osmosis (RO) is the leading technology globally. This method utilizes a semipermeable membrane that selectively transports ions between two reservoirs. In natural osmosis, water flows from a region of lower solute concentration to a region of higher concentration to achieve osmotic equilibrium. This process creates an osmotic pressure. To reverse this natural flow and thus achieve desalination, an external pressure must be applied to the more concentrated (saline) side. When this applied pressure exceeds the osmotic pressure, the water molecules are forced through the membrane, leaving the ions behind and effectively separating freshwater from the saline solution.

Currently, the most widely commercialized membranes are spiral-wound modules composed of ultrathin polyamide (PA) layers formed via in situ interfacial polymerization atop a microporous polysulfone (PFS) support and a polyester base.[6] The ultrathin PA layer provides adequate water permeability, high salt rejection, and operational stability across a broad pH range. However, several limitations have been identified in these systems. Notably, PA is susceptible to oxidative degradation by chlorine, which compromises the integrity of the selective layer.[7] Furthermore, biofouling, primarily due to the accumulation of microorgan-

isms, reduces membrane lifespan and results in significant losses in desalination performance.

Additionally, it is essential to note that polymeric membrane-based desalination technologies are approaching the thermodynamic efficiency limit, suggesting that further performance improvements may be marginal.

Carbon-based nanomaterials have been extensively investigated as filtration media due to their high selectivity and exceptional water permeability.[8–10] They also offer the possibility of surface functionalization through the incorporation of functional groups such as hydroxyl, carboxyl, epoxy, and amine, which can further enhance specific properties, as in the case of graphene oxide (GO).[11] In principle, the use of such nanomaterials is not intended to replace conventional polymeric membranes immediately, but rather to be integrated into existing membrane systems to improve performance, as exemplified by polyamide–graphene oxide (PA–GO) composite membranes.[12]

Molecular dynamics (MD) simulations have already demonstrated that, compared to conventional polymeric membranes, membranes incorporating two-dimensional materials exhibit water flux rates that are 2 to 3 orders of magnitude higher.[13] This exceptional permeability is attributed to the nanoscale confinement of water, which enhances its mobility, whether through the narrow diameters of nanotubes or nanopores, or through the openings in nanoslits.[14]

The presence of pores or slits in nano membranes induces water molecules to form an organized bound structure near the pore or slit, which facilitates fast mobility. This organization is structured in such a way that, in the presence of multiple pores, the water flow is additive,[15] not exhibiting the turbulence effect typically observed in pure polymeric structures. One of the crucial questions here is whether we can find a combination of distances and placements between membranes and slits that optimizes water flow in a multilayer organization of graphene oxide membranes.

In order to answer that question, we need to recognize that ion filtration in nanostructured membranes can occur via two primary mechanisms: (i) interlayer spacing in stacked

membrane structures, where water flows through the gaps between layers, or (ii) engineered nanopores that allow water to pass while selectively rejecting ions. In nanoporous membranes, the number, spacing, and geometry of pores can be tuned. For nanoslit-based membranes, key parameters include slit distance, size, and the commensurability between the slit dimensions and the solvated ions.

In this work, we test whether the water flow through slits in GO membranes is affected by the distance between the membranes and the alignment of the slits in each membrane. This study has applications in actual membranes of polyamide covered by GO surfaces, in which the slits are the defects of the coverage Systems consisting of saline water forced against adjacent graphene oxide membranes were simulated to replicate experimental conditions and provide atomistic insights into the impact of geometrical factors, such as commensurability and interlayer spacing. Notably, the experimental results indicate a change in water flux with specific configurations, findings further confirmed by simulations that show the impact of commensurability, slit width, and interlayer spacing on optimizing water passage. On the other hand, experimental results confirm the theoretical prediction of a lower impact of these conditions on salt rejection. The paper is organized as follows. In Section II, we introduce the experimental setup and computational details. In Section III, we present and discuss our results on water permeation, structural and dynamical aspects, and salt rejection in each system. Finally, a summary of our results and the conclusions are shown in Section IV.

Materials and Methods

This study combines experimental membrane characterization with MD simulations to investigate how graphene oxide membrane influences water and salt transport behavior across different length scales. The experimental procedures describe the preparation, coating, and testing of commercial RO modules, while the computational framework isolates the geometric parameters that control nanoscale water flow.

Experimental Setup

A GO dispersion was prepared at 100 mg $\cdot$ L^{-1} in a 50% v/v ethanol-water mixture and homogenized by sonication to promote a uniform distribution of the sheets. The pH of the dispersion was subsequently adjusted to 8.5 with a 0.1 mol $\cdot$ L^{-1} NaOH solution.

Commercial spiral RO modules (TW30-1812-75, active area 0.25 m^2) were modified *in situ*, without opening the elements, following a dynamic pressurization protocol from optimized procedures reported in the literature.[16] Before the modification step, each module was flushed with distilled water in recirculation mode for 30 min to remove preservatives and soluble residues. The GO dispersion was then circulated through the membrane module at 3.5 bar and a flow rate of 3.6 L$\cdot$$min^{-1}$ to prepare the modified membrane (GO-modified). To distinguish effects arising specifically from GO, control modules underwent the same pressurization and recirculation sequence using only the 50% v/v ethanol solution adjusted to pH 8.5 to prepare unmodified or pristine membranes.

Raman spectroscopy was used to characterize the chemical structure of the modified membranes. Measurements were performed on a WITec Alpha 300R confocal Raman system equipped with a 457 nm excitation laser (1-3 mW), acquiring five spectra at different locations on each sample at 20 °C. Surface morphology and nanometric features were examined by scanning electron microscopy (SEM, FEI Quanta 3D FEG) and atomic force microscopy (AFM, Cypher ES).

Membrane performance was evaluated both before and after GO treatment. Before testing, the spiral-wound elements were compacted with deionized water at 6 bar until a stable permeate flow was reached, after which hydraulic permeability and salt rejection experiments were conducted. Hydraulic permeability was determined by operating the system at pressures from 2 to 6 bar, keeping the feed flow rate constant at 2.4 L$\cdot$$min^{-1}$ with distilled water. The feed temperature was controlled at 25 $\pm$ 2 °C using a recirculating chiller. Permeate flow was recorded at each operating condition and normalized to 25 °C. The permeability coefficient (P) was obtained from the slope of the permeate flux versus applied pressure.[17]

To account for intrinsic variability among commercial RO elements, the relative permeability (P/P_0) was calculated as the ratio between the permeability after modification and the initial permeability.

Salt rejection experiments were performed using a 2.0 $g \cdot L^{-1}$ NaCl feed solution at 3.5 bar and 2.4 $L \cdot min^{-1}$. Rejection (R) was determined from the conductivity difference between feed and permeate streams following established procedures.[18]

Molecular Dynamics Details

Classical MD simulations were performed using the Large-scale Atomic/Molecular Massively Parallel Simulator (LAMMPS).[19] The systems were built with three adjacent graphene oxide membranes placed between two reservoirs, as shown in Figure 1(a): a feed reservoir, with all salt concentration, and a permeate reservoir. The sheets had an oxidation degree of 20%, with functional groups distributed as 2/3 hydroxyl (OH) and 1/3 epoxy (O). The number of molecules in the left reservoir was the same at the beginning for all systems. Graphene pistons were used as pressure controllers. We chose a salt concentration of approximately 0.5 M, which represents a value within the range of NaCl concentration in seawater.[20–22] Additionally, two different values of slit size (1.0 nm and 1.5 nm), inter-sheet distance (1.5 nm and 2.0 nm), and commensurability (high and low) were tested to evaluate the effect of geometric parameters on water flow behavior and salt rejection. Commensurability indicates how well two adjacent slits are aligned. Therefore, smaller values of b correspond to higher commensurability, as illustrated in Figure 1(b). The parameter b was set to 1.14 nm and 1.9 nm, corresponding to 50% and 70% spacing between the midlines of adjacent slits, relative to the total sheet height. The cross-sectional area of the systems is 14.82 nm^2. In Table 1, we present the eight systems identified from GO 1 to GO 8 according to their geometric properties, including slit size, interlayer spacing, and degree of commensurability.

In each simulation, the systems were first relaxed by a 1 ns energy minimization step performed in the NVT ensemble (constant number of particles, volume, and temperature).

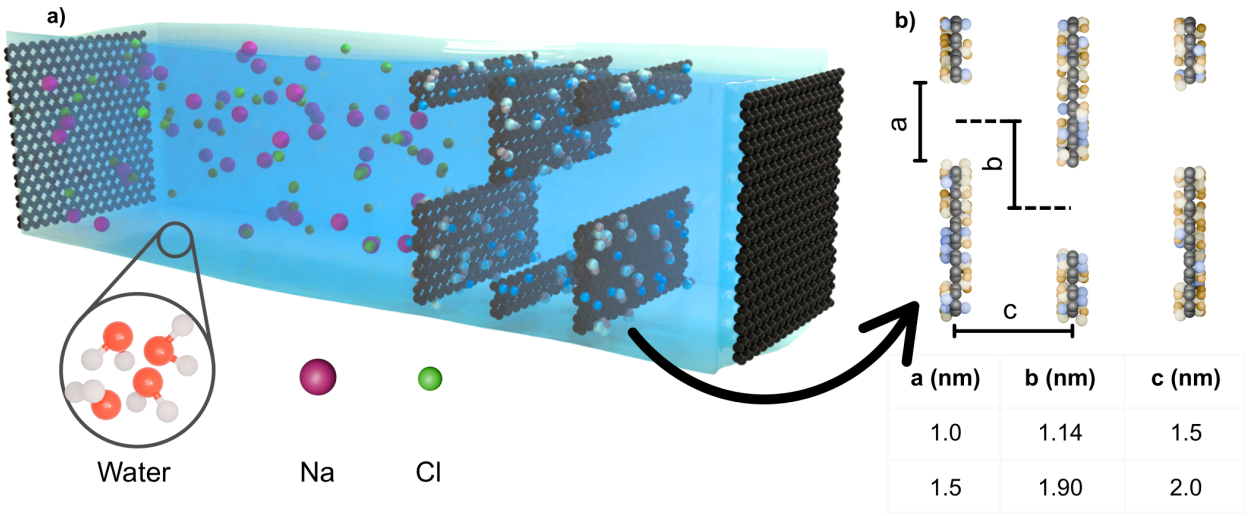

Figure 1: (a) Schematic representation of the simulation framework. On the left, we see the piston (graphene) pressing the ionic solution (water and NaCl) against the membrane. (b) Definition of the membrane's geometric parameters.

Table 1: Configurations showing slit size, interlayer spacing, and commensurability.

System	Slit size (nm)	Interlayer spacing (nm)	Commensurability
GO1	1.0	1.5	Low
GO2	1.0	1.5	High
GO3	1.0	2.0	Low
GO4	1.0	2.0	High
GO5	1.5	1.5	Low
GO6	1.5	1.5	High
GO7	1.5	2.0	Low
GO8	1.5	2.0	High

After minimization, an NPT ensemble (constant number of particles, pressure, and temperature) was applied by compressing the pistons until the water density stabilized around 1 g/cm^3. Then, a new NVT ensemble was used to equilibrate the system at the latest volume for 1 ns. Finally, an NPT ensemble was applied to create a non-equilibrium regime by unidirectionally pushing the pistons with a pressure gradient of 3000 bar until the spacing between the piston and the first layer reached 2 nm. Data were collected during this final stage. We used the SPC/E[23] water model and constrained the molecules with the SHAKE algorithm.[24] The timestep was set to 0.5 fs. The graphene oxide sheets were kept rigid,

and the temperature was set to 300 K using a Nosé–Hoover thermostat[25] with a damping time of 100 fs. The Lennard-Jones potentials and atomic charges used in the simulations are listed in Table 2. The particle-particle particle-mesh (PPPM) method was used to compute long-range electrostatic interactions beyond a 1.2 nm cutoff. We carried out five independent simulations for each system, collecting atomic trajectories every picosecond.

Table 2: Lennard-Jones parameters and atomic charges used in the simulations.

Atom type	σ (Å)	ε (kcal/mol)	Charge (e)
C (C-C)[26]	3.4	0.086	0
C (hydroxil)[27]	3.4	0.086	0.18
C (epoxy)[27]	3.4	0.086	0.18
O (hydroxyl)[27]	3.166	0.1553	−0.57
H (hydroxyl)[27]	0	0	0.39
O (epoxy)[27]	3.166	0.1553	−0.36
O (water)[28]	3.166	0.1553	−0.8476
H (water)[28]	0	0	0.4238
Na[29]	2.52	0.0347	1
Cl[29]	3.85	0.3824	−1

Results and discussion

Water transport through GO-modified membranes emerges from the interplay between surface organization, nanoscale confinement, and the chemical landscape imposed by GO. The following results highlight how these elements shape the movement of water and ions, revealing the conditions under which GO promotes enhanced flow while preserving selective transport.

Our assumption is that the decrease in the friction allow water to be more mobile and that this is generated by an organization of water molecules before approaching the nano slit due to the hydrogen bond network and the smooth nature of the GO surface. This hypothesis is tested here using experiments and simulations.

Pristine and GO Membranes: Experimental Results on Water and Salt Structure and Mobility

The pristine membrane, shown in Figure 2(a), exhibits a light and uniform surface with no visible markings or grooves. In contrast, the GO-modified is shown in Figure 2(b), displaying a pronounced change in appearance: well-defined grooves emerge across the surface, matching the geometry of the polymeric mesh used as the feed spacer in spiral-wound modules. Feed spacers play a crucial role in the performance of RO systems. Besides providing mechanical support and minimizing pressure drop, they create flow channels, reduce concentration polarization, and introduce controlled micro-turbulence that helps mitigate fouling and biofouling. The brownish coloration observed along the grooves of the GO-modified membrane suggests preferential deposition or accumulation of GO in these regions. This indicates that the transport and distribution of the modification dispersion inside the module are strongly influenced by the presence of the spacer, which directs the flow paths and locally enhances GO retention.

The presence of GO on the membrane surface is further supported by the Raman spectra shown in Figures 2(c) and 2(d). Two Raman shifts widely recognized as key identifiers of GO are highlighted by the vertical dashed lines in the spectra. The peak at $\sim$1360 cm^{-1} corresponds to the D band, which is associated with structural defects introduced by oxygen-containing functional groups such as epoxy, carbonyl, and hydroxyl groups. These disruptions in the sp^2-hybridized C-C network are characteristic of the oxidized and defect-rich structure of graphene oxide.[30] The G band, located near 1585 cm^{-1}, arises from the in-plane vibrational modes of sp^2-bonded carbon atoms and reflects the remaining ordered graphitic domains. The simultaneous appearance of both D and G bands in the modified membrane constitutes clear evidence of GO incorporation into the polymeric surface. In contrast, their absence in the pristine membrane confirms the lack of carbon-based nanomaterial prior to modification.

In addition to the GO-related bands, characteristic vibrational features of the underlying

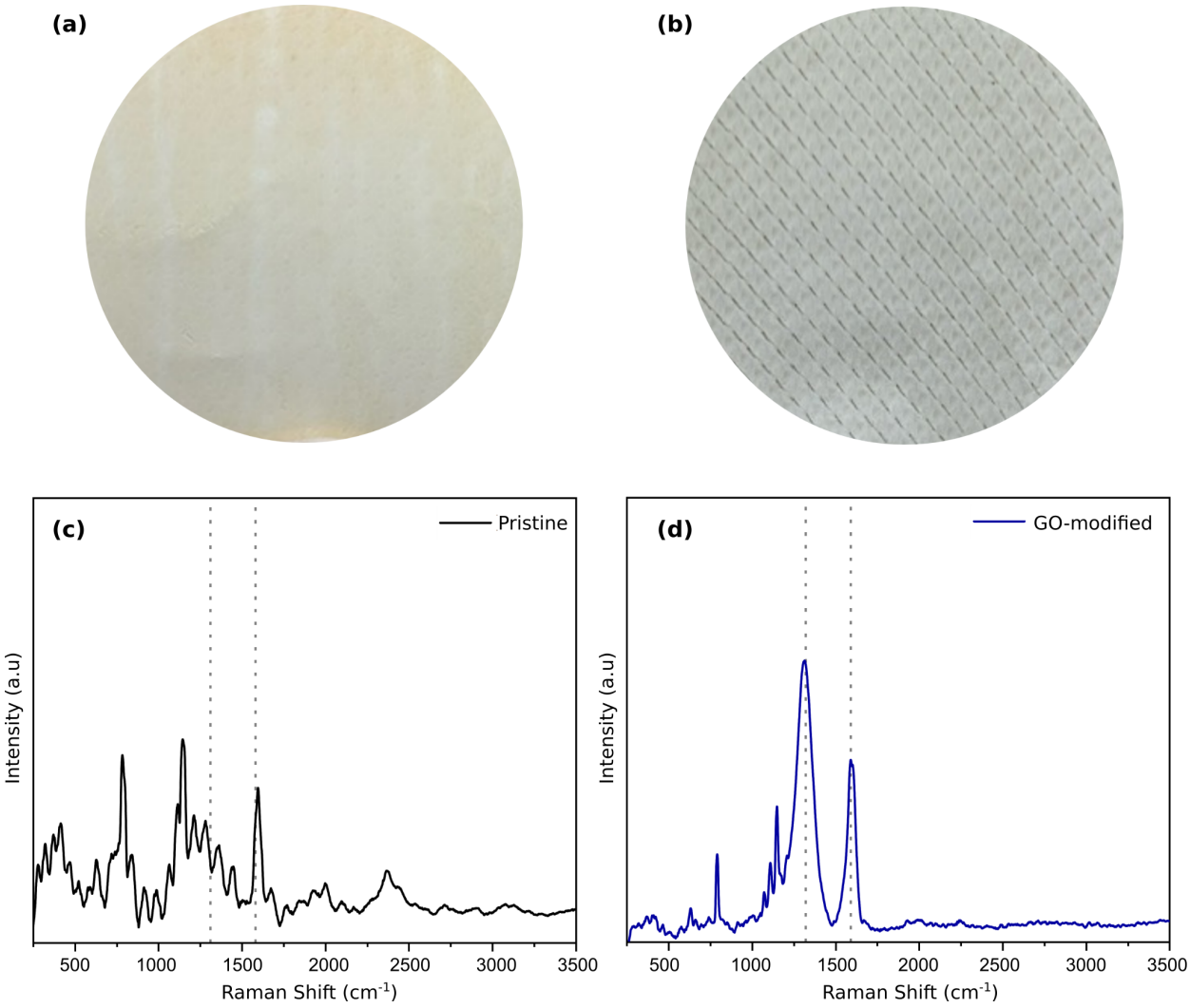

Figure 2: Optical microscopy images (16× magnification) and Raman spectra of the membranes (a,c) pristine and (b,d) GO-modified membranes.

membrane materials are also observed in all spectra. For the PA selective layer, bands appear at 634 cm^{-1} (CN vibration), at 1070 and 1109 cm^{-1} (C-C stretching), and at 1600-1608 cm^{-1} (amide group vibrations), consistent with previous reports.[31] Signals originating from the polysulfone (PSF) support layer are likewise present, including the distinctive band at 791 cm^{-1} attributed to Ar-S-Ar stretching and an additional peak at 1149 cm^{-1} corresponding to the symmetric stretching of the sulfone (SO_2) group.[32] The persistence of these PA and PSF features across all samples indicates that the GO deposition process does not alter the chemical structure of the base membrane. In contrast, the emergence of the D and G bands

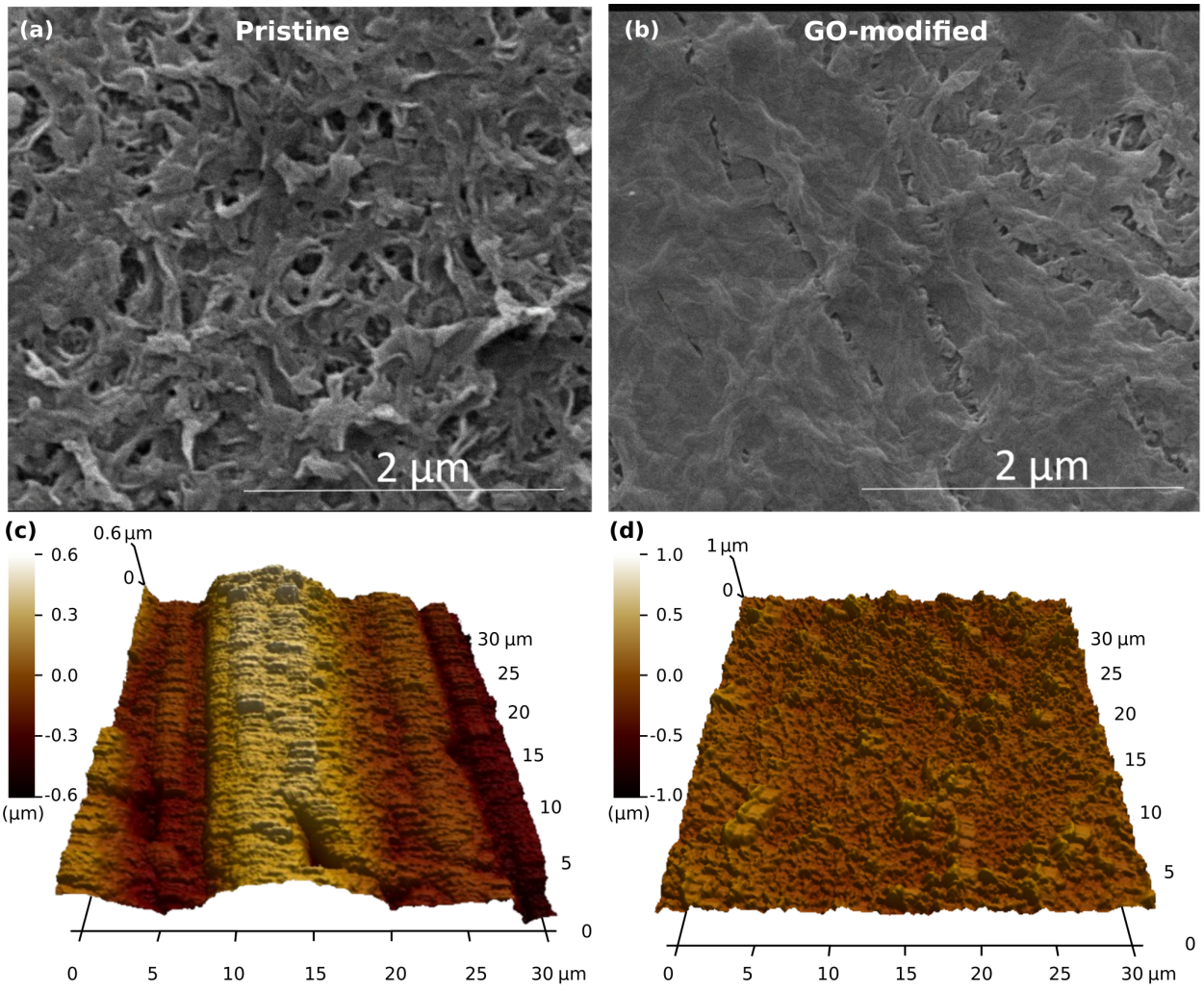

Figure 3: Scanning electron microscopy images of (a) the pristine and (b) the GO-modified membranes. Surface topography obtained by atomic force microscopy for (c) unmodified and (d) modified membranes.

uniquely in the modified membrane confirms the successful incorporation of GO.

The SEM image of the pristine membrane (Figure 3(a)) reveals a rough, nodular surface typical of polyamide dense layers formed via interfacial polymerization. These irregular structures are known to play a central role in water transport and solute rejection, as they define the selective morphology responsible for the membrane's performance in aqueous separation processes.[33] After the GO deposition, the surface morphology changes noticeably. As shown in Figure 3(b), the GO coating smooths out part of the irregularities observed in the unmodified membrane. This attenuation of the nodular features is consistent with previous

reports on GO-modified polyamide membranes, where the incorporation of GO increased surface hydrophilicity and introduced antifouling characteristics.[33–35]

Atomic force microscopy (AFM) images obtained in non-contact mode are presented in Figure 3(c,d), enabling a detailed analysis of surface topography and roughness. Polyamide membranes used in reverse osmosis typically exhibit a ridge-and-valley morphology, as shown in the pristine sample. The GO-coated membrane displays a reduced height variation compared to the unmodified membrane, leading to significantly lower roughness metrics, including maximum height, minimum height, root-mean-square roughness (R_q), and average roughness (R_a), as summarized in Table 3.

Table 3: Surface roughness parameters obtained from AFM analysis based on 786,432 data points.

AFM Parameters*	**Pristine**	**GO-modified**
R_a (nm)	200 ± 97	90 ± 37
R_q (nm)	283 ± 107	114 ± 80
$R_{\max}$ (nm)	990	637
$R_{\min}$ (nm)	$-1,248$	-580

* $N = 786,432$

One of the main effects of incorporating GO onto the membrane surface is altering its surface roughness profile. Previous studies have shown that the lamellar structure of GO enables it to occupy and level the valleys present on PA surfaces preferentially, leading to a pronounced reduction in roughness-related parameters.[36,37] This filling effect produces a smoother, more uniform topography, as confirmed by AFM and optical profilometry analyses. For the GO-modified membrane, the average roughness (R_a) decreased to zero, the lowest among all membranes evaluated. In addition, both the maximum and minimum roughness values were reduced, reinforcing the smoothing effect of GO deposition on the membrane surface.

Figure 4 presents the relative hydraulic permeability and salt rejection values for the pristine and GO-modified membranes. As expected, the salt rejection remained above 90% even after surface modification, indicating that the GO coating did not compromise the

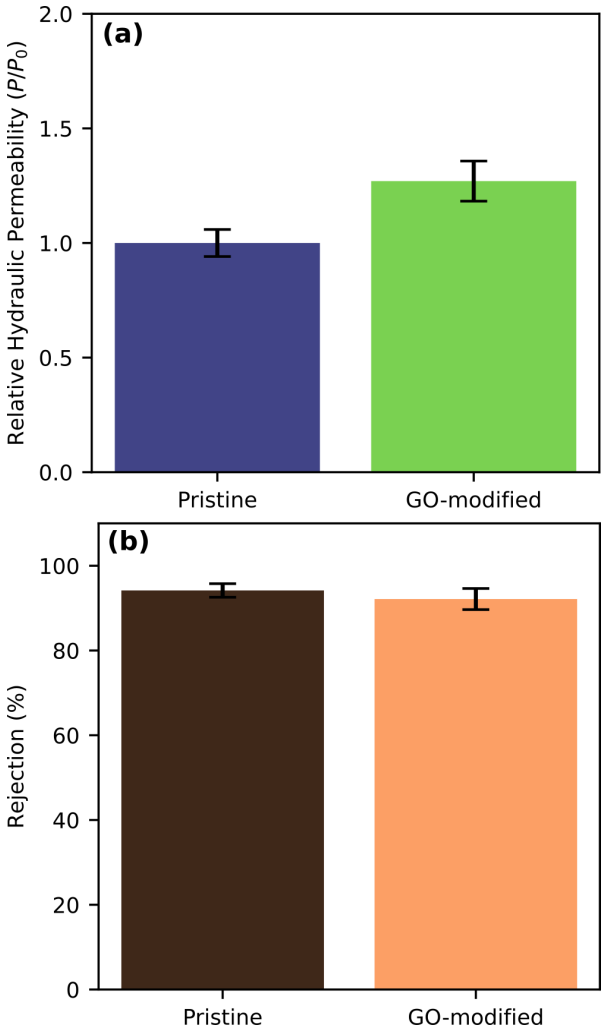

Figure 4: (a) Relative hydraulic permeability and (b) salt rejection for the pristine and GO-modified membranes.

integrity of the selective polyamide layer. In contrast, the hydraulic permeability increased by approximately 25% after GO deposition.

This enhancement is consistent with the widely discussed "frictionless channel" mechanism. According to this model, the hydrophilic edges and defect sites of GO nanosheets serve as entry points for water molecules. Once hydrated, molecules pass through these gate regions and move with increased mobility within the carbon-based nanocapillaries formed between adjacent GO sheets. The high water velocity is attributed to the extremely low friction at the water-graphitic interface, a phenomenon often referred to as drag-reduction or slip-flow behavior.[38]

Similar permeability enhancements have been reported by Bhoje *et al.*[39] who observed increases of comparable magnitude in thin-film composite reverse osmosis membranes modified with GO. Liu and Xu also reported that incorporating GO nanosheets onto polyamide surfaces led to sizable improvements in water flux within the same range, further supporting the mechanism proposed here.[12]

The experimental results presented thus far demonstrate that graphene oxide deposition significantly alters the membrane surface morphology and produces a marked enhancement in water flux without compromising salt rejection.

Although the literature proposes several plausible mechanisms, such as low-friction nanocapillaries and hydrophilic gate effects at the edges of GO nanosheets, none fully accounts for the superflow behavior observed in practice, and no consensus has yet been reached. To gain deeper insight into the molecular mechanisms governing this phenomenon and to isolate structural effects that cannot be directly probed in a spiral-wound module, the following section presents the theoretical analysis and molecular dynamics simulations developed for this study.

Simulation Results on Water and Salt Structure and Mobility in GO Membranes

Figures 5 and 6 show the overall distribution of water and the mobility of water and salt for each of the simulation cases presented in Table 1. Figure 5 shows that the slit size divides the system into two groups: a lower flow-rate group for 1.0 nm and a higher flow-rate group for 1.5 nm. A slight change in the slit aperture can cause a substantial increase in water permeation in these configurations. Indeed, previous studies have demonstrated that the opening size in a membrane is a decisive factor for water transport.[13,40]

The permeability shown in Figure 5(b) is a result of the linear fitting of the curves in Figure 5(a), which depicts the water flow rate during the simulations which is divided into two groups with higher and lower passage of water molecules in time. The consequence

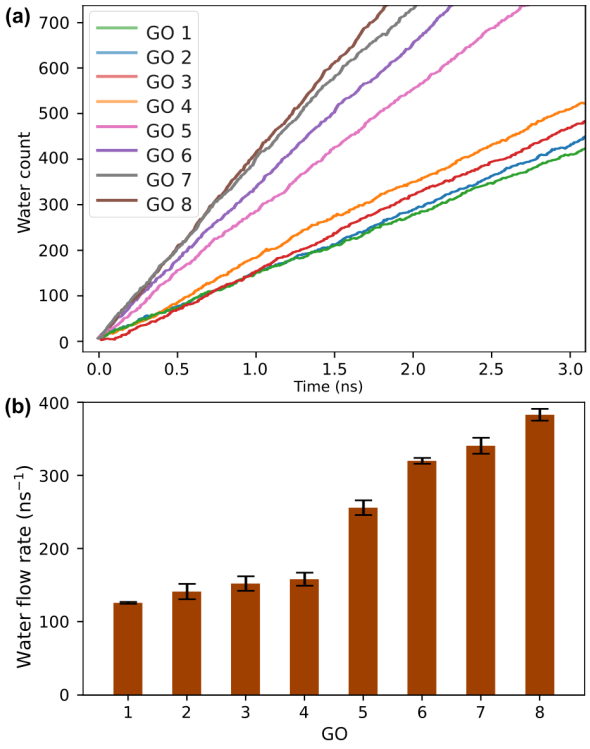

Figure 5: (a) The number of water molecules accumulated in the permeate reservoir during the pressure-driven part of the simulation as a function of time and (b) water flow rate for each system. The averages were obtained from five independent simulations.

can be visualized in Figure 5(b), where we observe a strong difference in the permeability between systems with 1.0 nm and 1.5 nm slit sizes.

In the former, there is a very slight increase in the flow rate from the GO1 to the GO4 system (all averages still within the standard deviations). In contrast, in the latter, there is an apparent linear increase in the water flow rate from the GO5 to the GO8 system.

The increase in permeability observed here is associated with the other two geometrical factors investigated in this contribution: the interlayer spacing and the commensurability. Among the 1.0 nm slit size systems, those with a 2.0 nm interlayer spacing, GO3 and GO4 systems, exhibit higher permeability (while still within the standard deviation) compared to those with a 1.5 nm spacing, GO1 and GO2 systems. A similar tendency is observed for 1.5 nm slit systems. Each system with a fixed slit size and interlayer spacing has a corresponding pair with either low or high commensurability. Systems with higher commensurability (even-

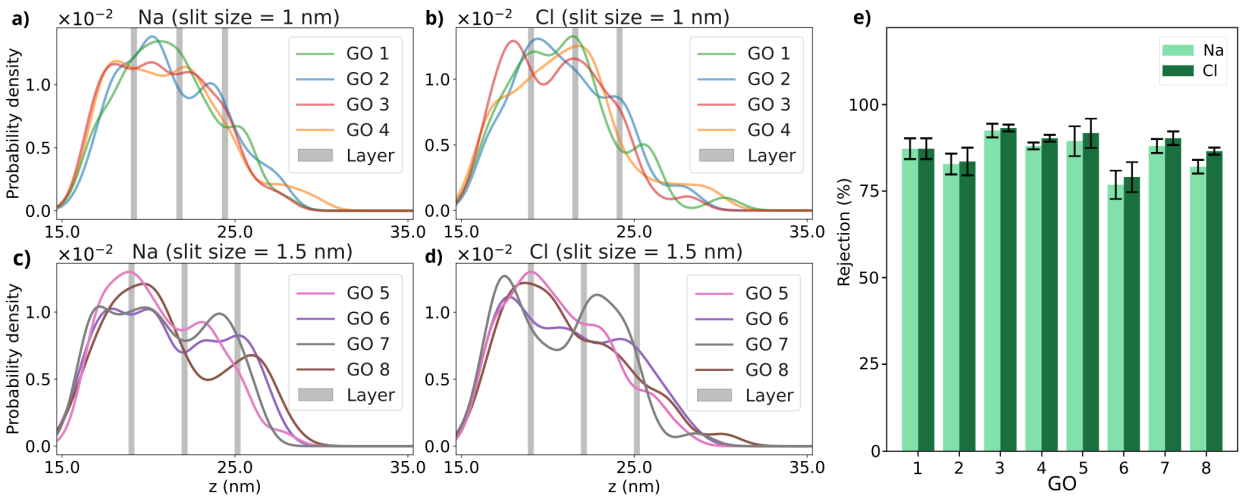

Figure 6: Averaged density distribution profiles for sodium (a,c) and chloride (b,d) as a function of the direction z and (e) ion rejection for each system. The averages were obtained from five independent simulations.

numbered systems) exhibit higher permeability compared to their counterparts with lower commensurability (odd-numbered systems).

In Figure 6(a-d), we show the salt distribution along the z-axis over the entire simulation time. Distinct behaviors are observed across all systems for both Na^+ and Cl^- species. The profiles exhibit peaks at different regions, suggesting possible non-local specificity in salt retention. More importantly, no preference for ion adsorption across the different geometries is observed, whereas all density profiles show similar occupation patterns and ion passage through the membranes.

The salt rejection (R), illustrated in the Figure 6(e), for each system was obtained from the following equation:

$$\mathrm{R} = \left(1 - \frac{\mathrm{C_i}}{\mathrm{C_f}}\right) \times 100\,, \tag{1}$$

where $\mathrm{C_f}$ is the salt ion concentration (Na^+ or Cl^-) in the feed reservoir and $\mathrm{C_i}$ is the concentration in the permeate reservoir.

In Figure 6(e), we plot the salt rejection for the sodium and chloride for the eight cases. It reveals that variations in slit size and interlayer spacing do not lead to significant changes in salt retention for either Na^+ or Cl^- species, even though Cl^- has a larger hydration radius

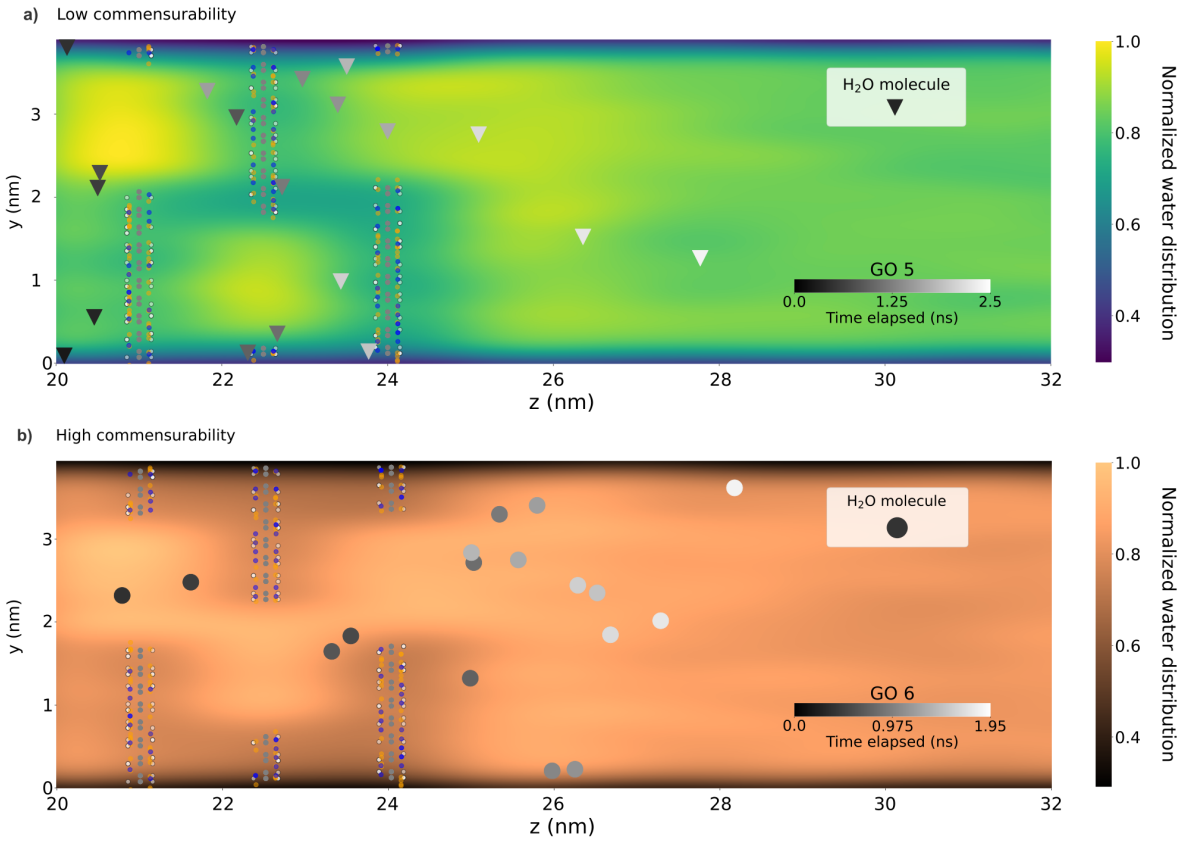

Figure 7: Lateral water distribution maps along the z-direction during the flow for the (a) GO5 (low commensurability) and (b) GO6 (high commensurability) systems. In detail, random water molecules are shown tracked over the time of a simulation for both systems.

compared to Na^+.[41] However, subtle changes can be observed in systems with a larger slit size. Additionally, increasing commensurability results in a slight but consistent decrease in salt rejection across the systems, suggesting that creating a more tortuous pathway primarily hinders salt transport. Comparable permeability and salt rejection behaviors have been observed in previous studies of similar graphene oxide multilayer systems.[42–44] The most significant difference is observed between the GO6 and GO5 systems, with a reduction of approximately 14% in Na^+ and 13% in Cl^- rejection. These results are essential because they elucidate the potential for enhancing water permeability while maintaining salt rejection.

While the differences in water permeability between 1.0 nm and 1.5 nm pores are clearly due to the larger area of entrance for water, the mechanism behind the differences in permeability when the pore size is the same but commensurability is varied is not clear. To

explore these distinctions, we analyze the colormaps in Figure 7.

Figure 7 shows the water distribution on the yz-plane over the entire simulation for GO5 in Figure 7(a) and GO6 in Figure 7(b). Among all the available systems, these exhibit the most significant variations in permeability and salt rejection as commensurability is varied, while keeping the slit size and interlayer spacing fixed. Water distribution exhibits a smoothed transition between the slits in the GO6 system, whereas GO5 shows small regions of lower water distribution between adjacent slits. It indicates that the increase in commensurability promotes a more homogeneous water distribution, which explains the higher water permeability observed for GO6 in Figure 5(b)

In both cases, as shown in Figure 8, well-localized regions of higher water probability density on the xy-plane can be observed before, inside, and after the slits in each sheet. The distributions suggest that water organizes itself at specific sites to move from the feed to the permeate reservoir. In other words, water molecules may establish preferential pathways as they flow through the slits. In fact, Nair et al.[45] have shown that water molecules in lamellar-type membranes display permeation mainly based on the interlayer gallery pathways.

To gain deeper insights into its structural dynamics, we analyzed the hydrogen bonds (HB) of the transported water molecules. These bonds are key to many of water's distinctive properties, driving a range of anomalies and playing a crucial role in various physical, chemical, and biological phenomena, including the formation and stability of numerous aqueous systems.[46–48]

In Figure 9(a), we show the average HB density between water molecules, during the pressure-driven flow regime. Compared to the reference value for bulk water, approximately 3.6 HBs per water molecule[49–51] (red dashed line), all systems exhibit lower averages, which is expected given the presence of ions[52,53] and the formation of HBs between water and the functional groups on the graphene oxide layers[54] (see Figure 9(c)). These factors hinder the structuring of the water HB.

Figure 9(a) shows an increase in the number of hydrogen bonds density between systems

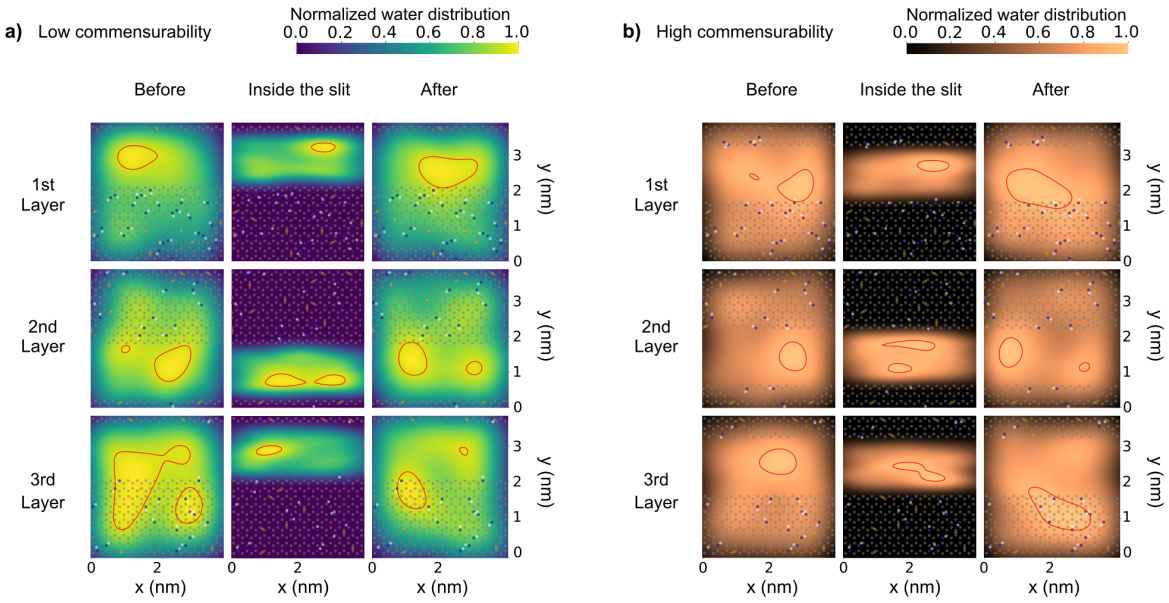

Figure 8: Water distribution maps across the cross-sectional plane, showing regions before, inside the slit, and after the membrane layers for (a) GO5 (low commensurability) and (b) GO6 (high commensurability). The regions enclosed by red lines correspond to areas with distribution intensity above 0.8.

with a 1.0 nm slit size (GO1-4) and those with a 1.5 nm slit size (GO5-8), which can be explained by the larger surface area of the graphene oxide membrane in the systems with narrower slits and, therefore, a larger number of functional groups. In addition, a decrease was observed in the number of HBs per water molecule inside the membrane region during the different time steps of the flow, with a stable count outside this region and before the flow (see Figure 9(b)). Although significant, this decrease does not continue indefinitely, reaching a stable behavior after approximately 40% of the total flow time. The confinement of the water flux can cause this geometric frustration through the channel created by the membranes.[55]

The implications of these results extend beyond the HB itself. In particular, the interaction of water with functional groups at the membrane surfaces may directly affect the mobility of molecules in different regions of the system. This connection becomes evident when analyzing the residence time correlation, which provides a quantitative measure of how long water remains confined near the membranes or within the slit regions.

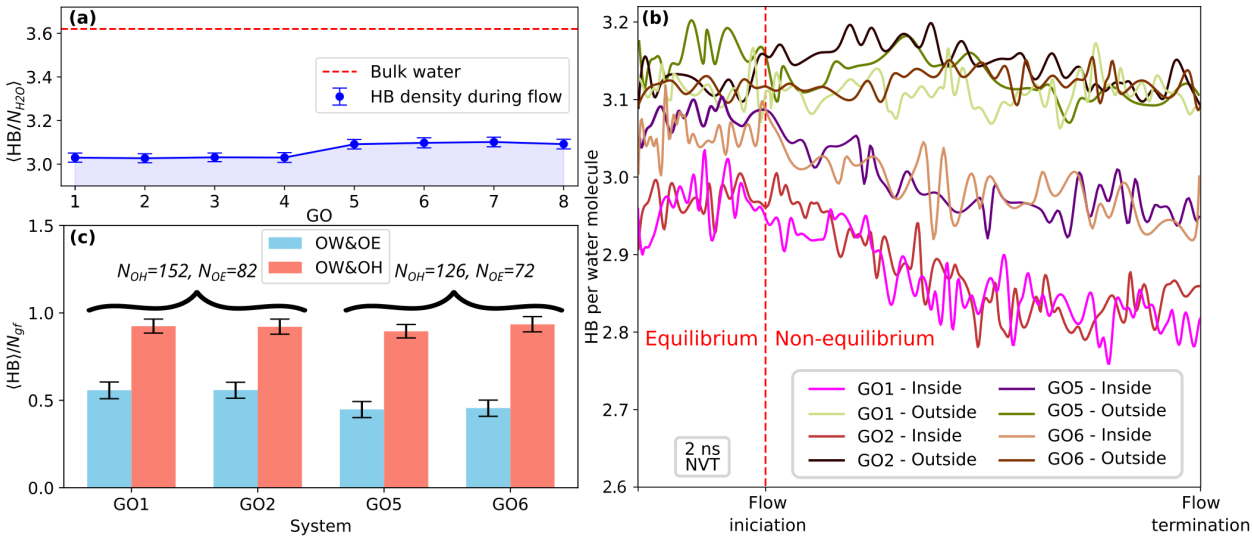

Figure 9: (a) The HB density of water for each system, (b) the number of HBs with functional groups for the GO1 and GO5 systems, and (c) the HB density of water within the region occupied by the membranes and outside this region for the GO1 and GO5 systems, respectively.

The residence time correlation is the probability that water molecules initially within a delimited region remain in that region over time. Evaluating the correlation between water residence profiles and residence times is extremely important for understanding various properties and the behavior of water in complex systems, as well as for obtaining accurate information on water wettability, anomalous diffusion, interactions between water molecules and their surrounding environment, and the relationship between these metrics and the system's non-equilibrium dynamics.[56]

Figure 10(a) shows the different regions defined for the residence time correlation analysis, representing volumes encompassing the membranes (odd-numbered regions) and volumes within the slits (even-numbered regions). The regions were configured using the box limits along the x and y-axes, while the z-axis limits were adjusted to ensure equal volumes across all regions. For the systems with smaller slits, GO1 and GO2, Figures 10(b) and (c), show that the residence time correlation exhibits a clear separation of decay rates between membrane and slit regions. For the larger slits (GO5 and GO6), Figures 10(d) and (e) indicate a less clear distinction between the residence time of the different regions.

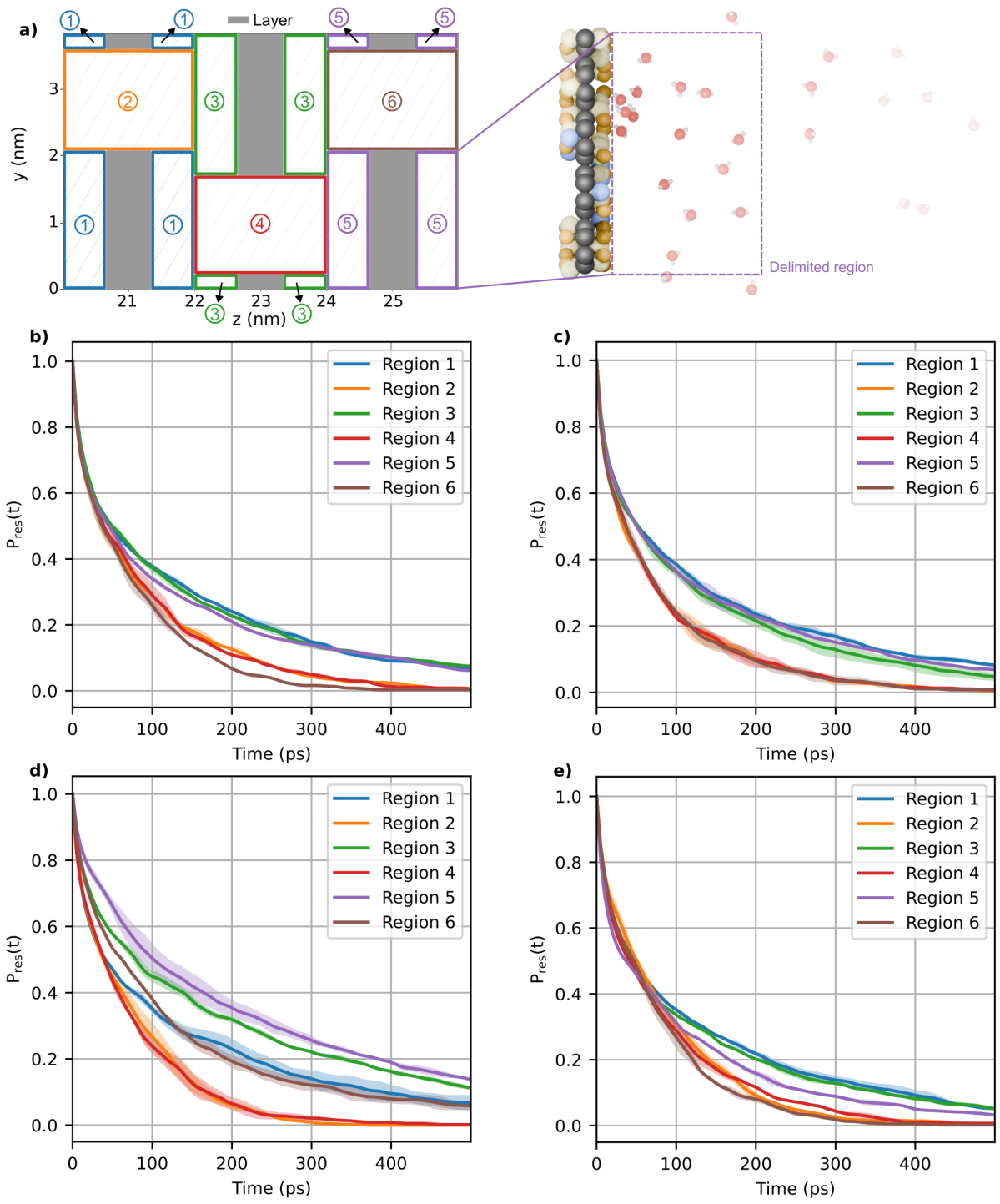

Figure 10: (a) Description of the delimited regions used for the calculation of water residence time, (b,c) residence probability profiles for the low commensurability system (GO1) and the high commensurability system (GO2), respectively, and (d,e) the profiles for the low commensurability system (GO5) and the high commensurability system (GO6), respectively. Shaded areas represent the standard deviation calculated from five independent datasets.

The fitted bi-exponential function,

$$P_{\text{res}}(t) = A\, e^{-t/\tau_1} + B\, e^{-t/\tau_2}, \tag{2}$$

yields the corresponding residence times τ_1 and τ_2. For normalized profiles, $A + B = 1$, where A and B are the amplitudes associated with each decay regime.

Figures 11(a) and (b) illustrate the residence times τ_1 and τ_2 for the smaller slit configurations GO1 and GO2 for each one of the six regions shown in the Figure 10(a). In this case, water molecules remain longer in membrane regions compared to slit regions, revealing a common spatial dependence of mobility. Comparing Figures 11(a) and (b) with Figure 8 we can see that longer residence times correspond to lower distribution of particles.

For systems with larger slits, GO5 and GO6 (Figures 10(d) and (e)), we observe a similar trend, with separation into two decay regimes. However, the curves for GO6 are closer together, suggesting greater variability across regions despite their shared spatial and structural characteristics. The residence times shown in Figures 11(c) and (d) confirm this trend, with both systems showing longer average retention in the membrane regions, but with higher differences in the mean values across similar regions. Interestingly, although GO5 and GO6 exhibit higher permeabilities when compared with the GO1 and GO2 systems, their residence times are not systematically shorter. This apparent decoupling highlights the role of commensurability between the slit geometry and the water structure: enhanced transport may arise not from reduced local residence, but from improved connectivity and cooperative pathways across the channels. In all systems, hydrogen bonds formed between water and the functional groups on the graphene oxide layers, see Figure 9(c), contribute to retaining water in the vicinity of the membranes, further explaining the consistently higher residence times in these regions.

In Figure 12, we illustrate the grouping of regions in each system, based on their amplitudes and characteristic residence times in each decay regime, which govern the probability of

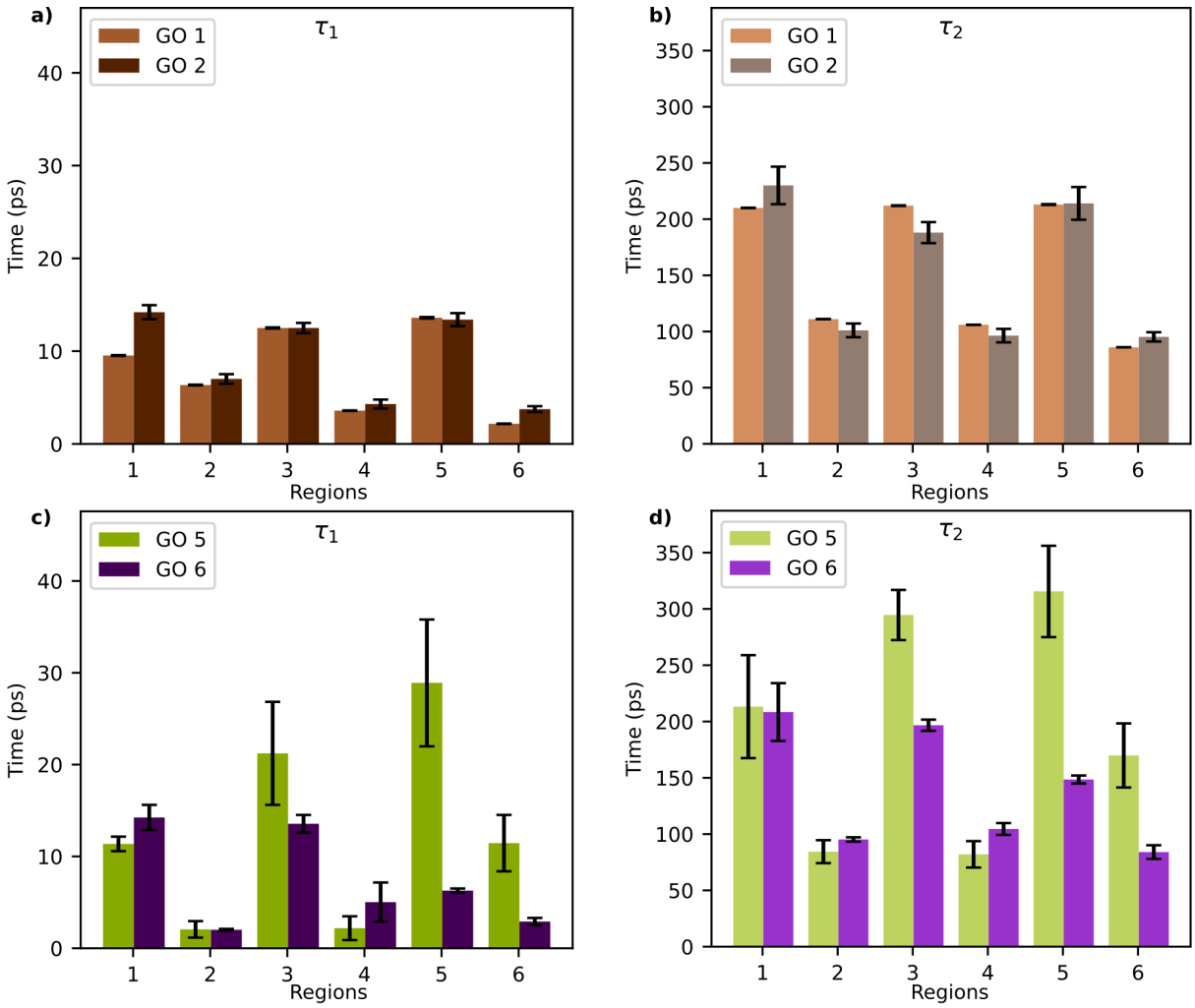

Figure 11: Residence times in the first (τ_1) and second (τ_2) decay regimes for GO1–2 (a,b) and GO5–6 (c,d) systems, across the regions defined in Figure 10(a). Error bars represent the standard deviation calculated from five independent datasets.

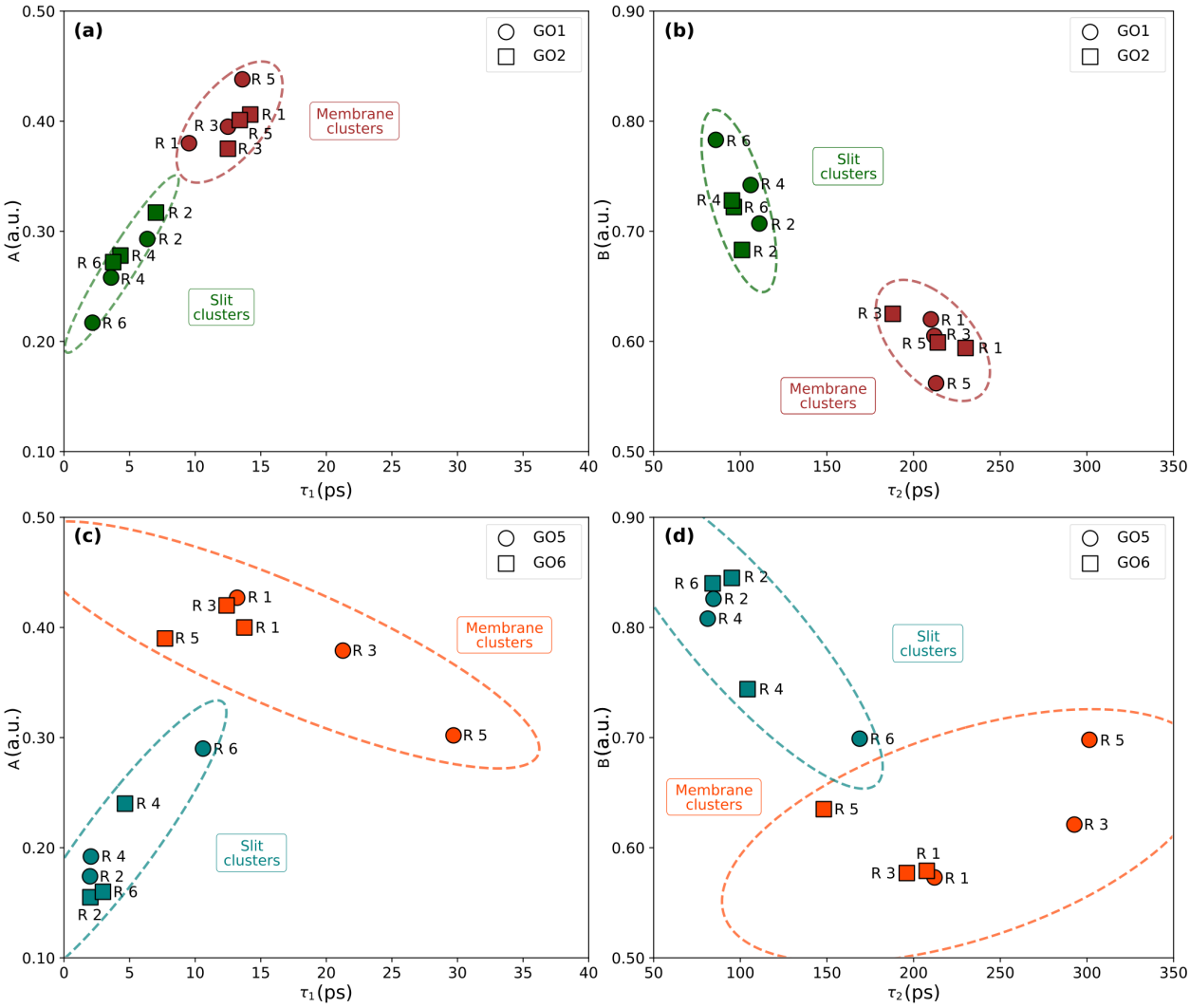

Figure 12: K-means clustering of regions based on parameters from the residence time probability decay regimes. Subfigures (a) and (b) show the analysis for the GO5-6 systems, using parameters from the first and second decay regimes, respectively. Subfigures (c) and (d) show the same analysis for the GO1-2 systems.

water molecules remaining in each region. These groupings were obtained using the k-means algorithm, a clustering method based on the optimization of the sum of squared Euclidean distances from each point to the nearest centroid, thereby minimizing the internal variation within each cluster (for more information, see the section about k-means analysis in the Supporting Information). In this analysis, the algorithm was set to find two groups per system.

From a general standpoint, in both decay regimes shown in Figure 12, k-means cluster-

ing consistently splits each system into two groups corresponding to the slit and membrane regions. These results confirm that common regional characteristics exert a similar influence on water-molecule displacement, regardless of commensurability. Although similar regions are well clustered in all available systems, thus confirming the regional separation, the clusters' compactness is significantly affected by the slit size. For the narrower slit systems with 1 nm, GO1 and GO2, the mean dispersion of the points from the centroid is notably lower (e.g., membrane cluster at the first decay regime: 1.11 ps^{-1} and slit cluster: 1.43 ps^{-1}; membrane cluster at the second decay regime: 8.11 ps^{-1} and slit cluster: 6.76 ps^{-1}), indicating that the residence time profiles for these systems, as shown in Figures 10(b) and (c), within each group (slit or membrane) are highly homogeneous. In comparison, for the systems with wider 1.5 nm slit, GO5 and GO6, the mean dispersion is considerably increased (e.g., membrane cluster at the first decay regime: 6.10 ps^{-1} and slit cluster: 2.40 ps^{-1}; membrane cluster at the second decay regime: 47.15 ps^{-1} and slit cluster: 22.36 ps^{-1}). This higher dispersion, or lower compactness, suggests that although the k-means method correctly classifies the regions, there is greater heterogeneity in the decay parameters across different slits and membranes. These results are expected due to the greater volume and, consequently, greater variation in water dynamics in the larger slits, reflected in a higher permeability.

The Taylor diagrams in Figure 13 display the Pearson correlation (corr), the centered root mean square (CRMS), and the standard deviation (σ) for each probability residence time profile across the GO1 and GO2. The analogous results for the GO5 and GO6 systems are presented in Figure S3 of the Supporting Information. The standard deviation reflects the variability of the curve values relative to their average, while the CRMS quantifies the difference in profile shape. From a general perspective, these diagrams consistently highlight the spatial dependence of water molecule dynamics, which is common to all systems. Strong correlations are observed among residence time probability profiles both within slit regions and among those associated with membrane regions. Importantly, the range of standard deviations is highly similar across the four systems – GO1 (0.167-0.191), GO2 (0.172-0.197),

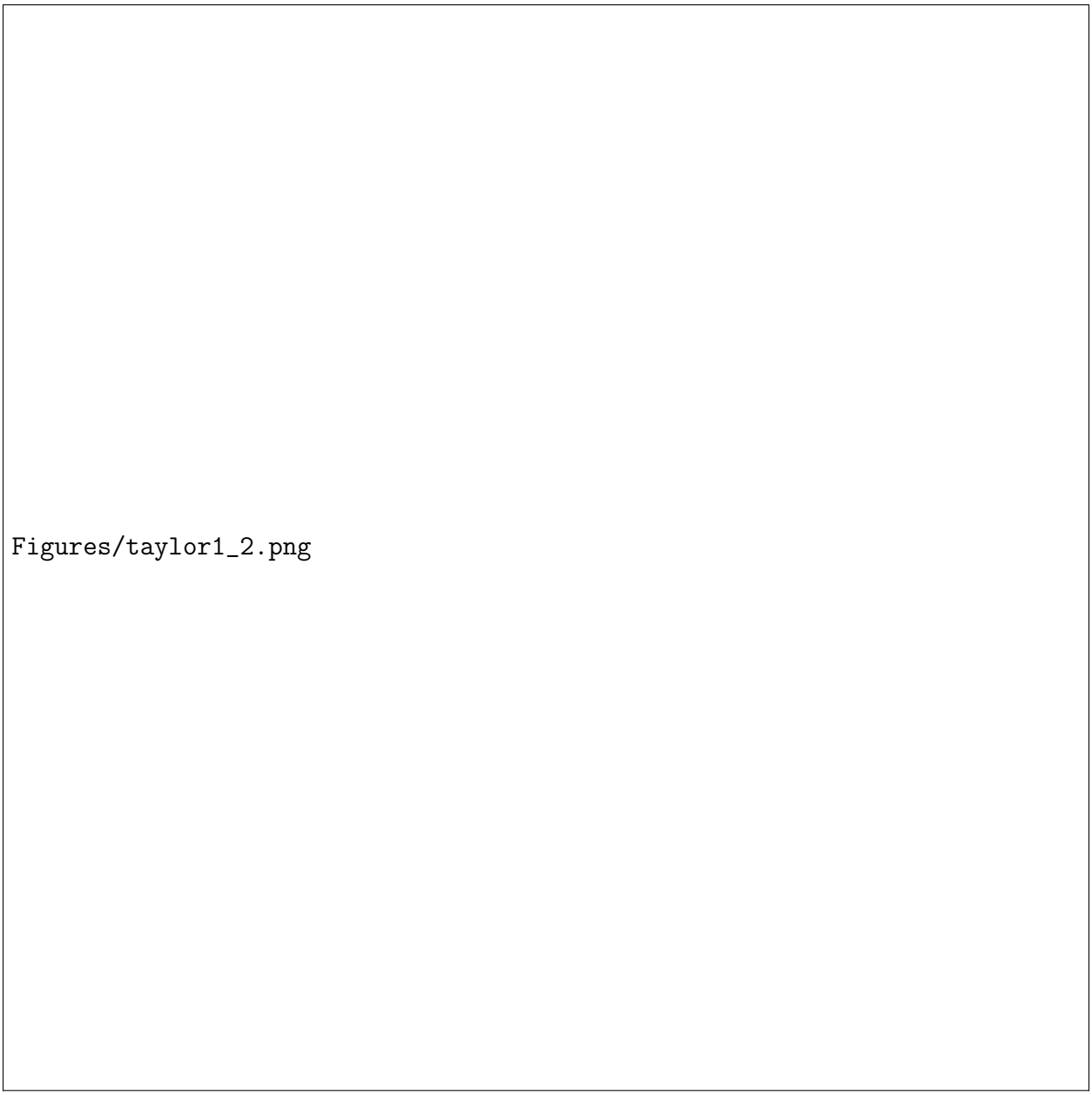

Figure 13: Taylor diagrams for each region in the GO1 system (a-f) and the GO2 system (g-l).

GO5 (0.173-0.197), and GO6 (0.172-0.209) – demonstrating comparable variability overall. The effect of the slit width is best observed by analyzing the CRMS and correlations between regions. The primary difference between the 1 nm slit size systems (GO1 and GO2) and the 1.5 nm systems (GO5 and GO6) lies in the degree of dynamic interdependence between the slit and membrane regions, as reflected by the CRMS. In the 1 nm slit systems, the intense confinement results in a lower CRMS in the slit region compared to the membrane region, indicating a coupled dynamic and profiles with a more unified shape. For instance, the $\mathrm{CRMS_{R5,R2}}$ (CRMS between Regions 5 and 2) is 0.0253 for GO1 and 0.0278 for GO2. In wider slit systems, the larger spacing allows the dynamics within the slits to decouple more significantly from those on the membrane surfaces. This manifests as significantly higher CRMS values (a larger difference in profile shape) when comparing slit and membrane regions: the $\mathrm{CRMS_{R5,R2}}$ is 0.0621 for GO5 (the highest among all systems) and 0.0410 for GO6. Regarding the correlation, the narrow slit systems maintain a robust correlation between slit and membrane regions (the minimum correlation is $\mathrm{corr_{R1,R6}} = 0.9757$ for GO1 and $\mathrm{corr_{R1,R4}} = 0.9867$ for GO2). However, the GO5 system exhibits the lowest correlation of all ($\mathrm{corr_{R5,R2}} = 0.9449$), which strongly suggests that the slit width increase, combined with poor commensurability, maximizes the dynamic decoupling. In contrast, the GO6 system exhibits higher correlations between slit and membrane regions (the minimum correlation is $\mathrm{corr_{R1,R2}} = 0.9870$), demonstrating that commensurability acts as a structural key factor, mitigating the decoupling effect of slit enlargement and maintaining a strong similarity in the behavior of the residence time profiles across regions. In fact, the flow magnitude is predominantly governed by the slit width. When moving from 1 nm to 1.5 nm, the lowest increase in mean permeability is approximately 97.85 $\mathrm{ns^{-1}}$, which is around three times larger than the maximum difference observed among any 1 nm systems. These results are consistent with the greater available volume and the increased dispersion of the k-means clusters observed for GO5 and GO6, indicating a higher volume of water with less confined, faster dynamics in the larger slits, thereby boosting the overall flow rate. Within each slit width, the high

commensurability significantly increases permeability compared to the systems with lower commensurability. From GO1 to GO2, commensurability increases the permeability by approximately 12%, whereas from GO5 to GO6, the increase is approximately 25%. This gain in permeability is intimately connected to the homogeneity and dynamic coupling quantified in the Taylor analysis. The local behavior is also more expressive in wider slit systems. Although GO5 has a wider slit, its permeability is significantly lower than that of GO6 due to its greater dynamic heterogeneity. The higher correlation values and the lower CRMS between slit and membrane regions observed in the GO6 system, relative to GO5, indicate that the decoordination of water molecules during flow, caused by the slit enlargement, is diminished by the increase in commensurability. In other words, dynamic bottlenecks that act as critical points with high resistance to flow, thereby strangling the global flow and decoupling the slit-membrane dynamics, are mitigated by increased commensurability.

Combining Experimental and Simulation Results

The theoretical results reveal that subtle variations in nanoscale confinement, such as slit width, interlayer spacing, and commensurability between adjacent slits, significantly influence water structuring, hydrogen-bond dynamics, and residence-time distributions within the confined regions. These effects, which cannot be individually controlled in the experimental module, help explain how preferential flow pathways emerge and how specific structural arrangements can either amplify or hinder water transport. The observed relationship between increased commensurability and enhanced permeability supports the idea that aligned GO regions, similar to those formed along the spacer-induced grooves seen experimentally, can act as high-flux domains.

Furthermore, the simulations show that increasing the slit width and interlayer spacing yields substantial gains in water permeability while maintaining ion rejection, a behavior entirely consistent with the experimental findings. The formation of extended low-friction pathways, combined with hydration-shell exclusion for ions, constitutes a fundamental mech-

anism underlying this trend. As such, the theoretical analysis provides a clear molecular-level explanation for the approximately 25% increase in hydraulic permeability observed in the GO-modified membrane.

Finally, the evaluation of hydrogen-bond networks and residence-time clustering indicates that GO surfaces promote regions of reduced confinement and enhanced water mobility, reinforcing the "frictionless channel" hypothesis frequently invoked in the literature. The combination of GO-induced structural alignment, surface smoothing, and altered water organization at the GO–polyamide interface suggests that the observed superflow likely arises from a collective, synergistic effect rather than a single isolated mechanism. In this way, integrating experimental evidence with theoretical modeling yields a coherent and comprehensive picture of the role of GO in water transport, providing a solid foundation for the rational design of next-generation high-performance membranes.

Conclusions

In this paper, we analyze the permeability of water and the rejection of salt when using a desalination membrane. Our assumption is that the GO membrane allows water to be structured, which enhances permeability, while polymeric membranes, such as pristine polyamide, promote disorganization, particularly at high pressures, thereby decreasing permeability.

First, this assumption is tested experimentally using both a pure polymeric membrane and a membrane covered by GO. The experimental findings demonstrate that the incorporation of GO onto commercial polyamide membranes produces three key effects: (i) a clear modification of the surface morphology, with GO preferentially accumulating along the spacer-imprinted grooves; (ii) a substantial reduction in surface roughness, resulting in a smoother and more uniform topography; and (iii) a marked enhancement of hydraulic permeability of approximately 25%, while salt rejection remains above 90%. These observations confirm that GO effectively reorganizes the membrane surface without compromising its se-

lective polyamide layer, enabling fast water transport through regions of reduced friction and improved hydrophilicity.

The theoretical and MD analyses further reveal that water mobility within GO-based nanochannels is highly sensitive to geometric parameters, including slit width, interlayer spacing, and commensurability between adjacent slits. Wider slits and larger interlayer distances increase the available free volume and accelerate transport, while high commensurability promotes dynamic coupling across similar regions, suppresses bottlenecks, and enhances global water flux. The MD simulations also show that water molecules develop preferential pathways, undergo significant network destructuring within the membrane region, and experience strong spatial dependence of residence times, all signatures of complex nanoscale transport behavior modulated by GO morphology.

The experimental and theoretical results converge toward a unified mechanistic picture. The experimentally observed enhancement in membrane permeability is closely aligned with the molecular-scale mechanisms revealed in the simulations: low-friction pathways forming between GO sheets, structural alignment that improves connectivity between channels, and modified hydrogen-bond environments that facilitate rapid water mobility. This synergy provides a comprehensive explanation for how GO modifies transport pathways without compromising ionic exclusion. Beyond elucidating the mechanisms underlying the observed superflow, these combined results establish a solid framework for the rational design of next-generation desalination membranes in which nanoscale geometry and macroscopic performance are jointly optimized.

Acknowledgement

The authors thank Petrobras, Minas Gerais Research Support Foundation (FAPEMIG), National Council for Scientific and Technological Development (CNPq), and the Center of Microscopy at the Federal University of Minas Gerais (`http://www.microscopia.ufmg.br`) for providing the equipment and technical support for experiments involving electron microscopy. The authors also acknowledge the CPAD-UFSM and CENAPAD-SP for the computational time. M.L.P.J acknowledges financial support from FAPDF (grant 00193-00001807/2023-16), CNPq (grants 444921/2024-9 and 308222/2025-3), and CAPES (grant 88887.005164/2024-00). M.C.B. and M.H.K. thank CNPq for the Universal grant No. 405479/2023-9. P.A.N. acknowledges financial support from CNPq grant 307106/2021-7. This work was carried out with the support of the Coordination for the Improvement of Higher Education Personnel - Brazil (CAPES) - Financing Code 001.

Supporting Information Available

The Supporting Information is available free of charge at https://pubs.acs.org/ containing information regarding the water flux through the graphene oxide membranes, ionic density profiles, color maps, and Taylor diagrams.

References

(1) Veldkamp, T.; Wada, Y.; Aerts, J.; Döll, P.; Gosling, S. N.; Liu, J.; Masaki, Y.; Oki, T.; Ostberg, S.; Pokhrel, Y.; others Water scarcity hotspots travel downstream due to human interventions in the 20th and 21st century. *Nature communications* **2017**, *8*, 15697.

(2) Mekonnen, M. M.; Hoekstra, A. Y. Four billion people facing severe water scarcity. *Science advances* **2016**, *2*, e1500323.

(3) Jones, E.; Qadir, M.; van Vliet, M. T.; Smakhtin, V.; Kang, S.-m. The state of desalination and brine production: A global outlook. *Science of the Total Environment* **2019**, *657*, 1343–1356.

(4) Uhlenbrook, S.; Connor, R.; others The United Nations world water development report 2019: leaving no one behind. *United Nations Educational, Scientific and Cultural Organization,* **2019**, *7*, 1–201.

(5) Elimelech, M.; Phillip, W. A. The future of seawater desalination: energy, technology, and the environment. *science* **2011**, *333*, 712–717.

(6) Khorshidi, B.; Thundat, T.; Fleck, B. A.; Sadrzadeh, M. A novel approach toward fabrication of high performance thin film composite polyamide membranes. *Scientific reports* **2016**, *6*, 1–10.

(7) Kucera, J. Biofouling of polyamide membranes: Fouling mechanisms, current mitigation and cleaning strategies, and future prospects. *Membranes* **2019**, *9*, 111.

(8) Boretti, A.; Al-Zubaidy, S.; Vaclavikova, M.; Al-Abri, M.; Castelletto, S.; Mikhalovsky, S. Outlook for graphene-based desalination membranes. *npj Clean Water* **2018**, *1*, 5.

(9) Heiranian, M.; Farimani, A. B.; Aluru, N. R. Water desalination with a single-layer MoS2 nanopore. *Nature communications* **2015**, *6*, 8616.

(10) Köhler, M. H.; Bordin, J. R.; de Matos, C. F.; Barbosa, M. C. Water in nanotubes: The surface effect. *Chem. Eng. Sci.* **2019**, *203*, 54–67.

(11) Dehaghani, M. Z.; Mashhadzadeh, A. H.; Vafa, N.; Firoozabadi, B.; Nouranian, S.; Golman, B.; Spitas, C. Evaluation of water desalination performances of functionalized nanoporous graphene membranes by molecular dynamics simulation. *Computational Materials Science* **2023**, *228*, 112308.

(12) Liu, Q.; Xu, G.-R. Graphene oxide (GO) as functional material in tailoring polyamide thin film composite (PA-TFC) reverse osmosis (RO) membranes. *Desalination* **2016**, *394*, 162–175.

(13) Cohen-Tanugi, D.; Grossman, J. C. Water desalination across nanoporous graphene. *Nano lett.* **2012**, *12*, 3602–3608.

(14) Bordin, J. R.; Diehl, A.; Barbosa, M. C. Relation between flow enhancement factor and structure for core-softened fluids inside nanotubes. *J. Phys. Chem. B* **2013**, *117*, 7047–7056.

(15) Kleinubing Abal, J. P.; Barbosa, M. C. Molecular fluid flow in MoS2 nanoporous membranes and hydrodynamics interactions. *J. Chem. Phys.* **2021**, *154*, 134506.

(16) Oliveira, C.; dos Santos, R.; Viegas, J.; Souza, R.; Silva, R.; Pinto, H.; Viana, M.; Amaral, M.; de Vasconcelos, C.; Silva, G. In situ graphene oxide surface modification of spiral-wound RO membranes for enhanced chlorine resistance and antifouling performance. *Journal of Water Process Engineering* **2025**, *79*, 109060.

(17) de Oliveira, C. P. M.; Viana, M. M.; Silva, G. R.; Lima, L. S. F.; de Paula, E. C.; Amaral, M. C. S. Potential use of green TiO2 and recycled membrane in a photocatalytic

membrane reactor for oil refinery wastewater polishing. *Journal of Cleaner Production* **2020**, *257*, 120526.

(18) Shao, F.; Su, X.; Shen, X.; Ren, S.; Wang, H.; Yi, Z.; Xu, C.; Yu, L.; Dong, L. Highly improved chlorine resistance of polyamide reverse membrane by grafting layers of graphene oxide. *Separation and Purification Technology* **2021**, *254*, 117586.

(19) Thompson, A. P.; Aktulga, H. M.; Berger, R.; Bolintineanu, D. S.; Brown, W. M.; Crozier, P. S.; in 't Veld, P. J.; Kohlmeyer, A.; Moore, S. G.; Nguyen, T. D.; Shan, R.; Stevens, M. J.; Tranchida, J.; Trott, C.; Plimpton, S. J. LAMMPS - a flexible simulation tool for particle-based materials modeling at the atomic, meso, and continuum scales. *Comp. Phys. Comm.* **2022**, *271*, 108171.

(20) Dhavamani, J.; Beck, A. J.; Gledhill, M.; El-Shahawi, M. S.; Kadi, M. W.; Ismail, I. M.; Achterberg, E. P. The effects of salinity, temperature, and UV irradiation on leaching and adsorption of phthalate esters from polyethylene in seawater. *Science of The Total Environment* **2022**, *838*, 155461.

(21) Zinke, J.; Nilsson, E. D.; Zieger, P.; Salter, M. E. The Effect of Seawater Salinity and Seawater Temperature on Sea Salt Aerosol Production. *Journal of Geophysical Research: Atmospheres* **2022**, *127*.

(22) Wang, Y.; He, Z.; Gupta, K. M.; Shi, Q.; Lu, R. Molecular dynamics study on water desalination through functionalized nanoporous graphene. *Carbon* **2017**, *116*, 120–127.

(23) Berendsen, H.-J.-C.; Grigera, J.-R.; Straatsma, T. P. The missing term in effective pair potentials. *J. Phys. Chem.* **1987**, *91*, 6269–6271.

(24) Ryckaert, J.-P.; Ciccotti, G.; Berendsen, H. J. Numerical Integration of the Cartesian Equations of Motion of a System with Constraints: Molecular Dynamics of n-Alkanes. *J. Comput. Phys.* **1977**, *23*, 327–341.

(25) Nosé, S. A Molecular Dynamics Method for Simulations in the Canonical Ensemble. *Mol. Phys.* **1984**, *52*, 255.

(26) Hummer, G.; Rasaiah, J. C.; Noworytra, J. P. Water conduction through the hydrophobic channel of a carbon nanotube. *Nature* **2001**, *404*, 188.

(27) Stauffer, D.; Dragneva, N.; Floriano, W.; Mawhinney, R.; Fanchini, G.; French, S.; Rubel, O. An atomic charge model for graphene oxide for exploring its bioadhesive properties in explicit water. *J. Chem. Phys.* **2014**, *141*.

(28) Berendsen, H. J. C.; Grigera, J. R.; Straatsma, T. P. The missing term in effective pair potentials. *J. Phys. Chem.* **1987**, *91*, 6269–6271.

(29) Fuentes-Azcatl, R.; Barbosa, M. C. Sodium Chloride, NaCl/ϵ: New Force Field. *J. Phys. Chem. B* **2016**, *120*, 2460–2470.

(30) Perreault, F.; Tousley, M. E.; Elimelech, M. Thin-film composite polyamide membranes functionalized with biocidal graphene oxide nanosheets. *Environmental Science & Technology Letters* **2014**, *1*, 71–76.

(31) Souza, M. L. d.; Moscardini, S. B.; Faria, E. H. d.; Ciuffi, K. J.; Rocha, L. A.; Nassar, E. J.; Silva, J. V.; Oliveira, M. F.; Maia, I. A. Óxido de ítrio e alumínio dopado com Yb3+ e Er3+ incorporado em membrana de poliamida. *Química Nova* **2018**, *41*, 519–527.

(32) Deimede, V.; Voyiatzis, G.; Kallitsis, J.; Qingfeng, L.; Bjerrum, N. Miscibility behavior of polybenzimidazole/sulfonated polysulfone blends for use in fuel cell applications. *Macromolecules* **2000**, *33*, 7609–7617.

(33) Xia, S.; Yao, L.; Zhao, Y.; Li, N.; Zheng, Y. Preparation of graphene oxide modified polyamide thin film composite membranes with improved hydrophilicity for natural organic matter removal. *Chemical Engineering Journal* **2015**, *280*, 720–727.

(34) Cho, Y. H.; Han, J.; Han, S.; Guiver, M. D.; Park, H. B. Polyamide thin-film composite membranes based on carboxylated polysulfone microporous support membranes for forward osmosis. *Journal of membrane science* **2013**, *445*, 220–227.

(35) Han, G.; Zhang, S.; Li, X.; Widjojo, N.; Chung, T.-S. Thin film composite forward osmosis membranes based on polydopamine modified polysulfone substrates with enhancements in both water flux and salt rejection. *Chemical Engineering Science* **2012**, *80*, 219–231.

(36) Salahshoori, I.; Seyfaee, A.; Babapoor, A. Recent advances in synthesis and applications of mixed matrix membranes. *Synthesis and Sintering* **2021**, *1*, 1–27.

(37) Croll, H.; Soroush, A.; Pillsbury, M. E.; Castrillón, S. R.-V. Graphene oxide surface modification of polyamide reverse osmosis membranes for improved N-nitrosodimethylamine (NDMA) removal. *Separation and Purification Technology* **2019**, *210*, 973–980.

(38) Castelletto, S.; Boretti, A. Advantages, limitations, and future suggestions in studying graphene-based desalination membranes. *RSC advances* **2021**, *11*, 7981–8002.

(39) Bhoje, R.; Ghosh, A. K.; Nemade, P. R. Development of performance-enhanced graphene oxide-based nanostructured thin-film composite seawater reverse osmosis membranes. *ACS Applied Polymer Materials* **2022**, *4*, 2149–2159.

(40) Köhler, M. H.; Bordin, J. R.; Barbosa, M. C. 2D nanoporous membrane for cation removal from water: Effects of ionic valence, membrane hydrophobicity, and pore size. *J. Chem. Phys.* **2018**, *148*, 222804.

(41) Zhou, J.; Lu, X.; Wang, Y.; Shi, J. Molecular dynamics study on ionic hydration. *Fluid Phase Equilibria* **2002**, *194-197*, 257–270.

(42) Chen, C.; Zhang, L. Effects of structural parameters on the desalination performance of a multilayer stacked graphene oxide membrane: insights from molecular dynamics simulation. *Nanoscale* **2025**, *17*, 12868–12879.

(43) Alinia, Z.; Akbarzadeh, H.; Zonoz, F. M.; Tayebee, R. Enhancing the seawater desalination performance of multilayer reduced graphene oxide membranes by introducing in-plane nanopores: a molecular dynamics simulation study. *Physical Chemistry Chemical Physics* **2024**, *26*, 9722–9732.

(44) Chen, B.; Jiang, H.; Liu, X.; Hu, X. Molecular Insight into Water Desalination across Multilayer Graphene Oxide Membranes. *ACS Applied Materials & Interfaces* **2017**, *9*, 22826–22836.

(45) Nair, R. R.; Wu, H. A.; Jayaram, P. N.; Grigorieva, I. V.; Geim, A. K. Unimpeded Permeation of Water Through Helium-Leak–Tight Graphene-Based Membranes. *Science* **2012**, *335*, 442–444.

(46) Djikaev, Y.; Ruckenstein, E. The variation of the number of hydrogen bonds per water molecule in the vicinity of a hydrophobic surface and its effect on hydrophobic interactions. *Current Opinion in Colloid & Interface Science* **2011**, *16*, 272–284.

(47) Reid, K. M.; Poudel, H.; Leitner, D. M. Dynamics of Hydrogen Bonds between Water and Intrinsically Disordered and Structured Regions of Proteins. *The Journal of Physical Chemistry B* **2023**, *127*, 7839–7847, PMID: 37672685.

(48) Hou, Y.; Wang, M.; Chen, X.; Hou, X. Continuous water-water hydrogen bonding network across the rim of carbon nanotubes facilitating water transport for desalination. *Nano Research* **2021**, *14*, 2171–2178.

(49) Thompson, H.; Soper, A. K.; Ricci, M. A.; Bruni, F.; Skipper, N. T. The Three-Dimensional Structure of Water Confined in Nanoporous Vycor Glass. *The Journal of Physical Chemistry B* **2007**, *111*, 5610–5620, PMID: 17472364.

(50) Chava, B. S.; Das, S. Strength, number, and kinetics of hydrogen bonds for water confined inside boron nitride nanotubes. *Nanoscale Adv.* **2024**, *6*, 3329–3337.

(51) Kumar, R.; Schmidt, J. R.; Skinner, J. L. Hydrogen bonding definitions and dynamics in liquid water. *The Journal of Chemical Physics* **2007**, *126*, 204107.

(52) Di Lecce, S.; Albrecht, T.; Bresme, F. Taming the thermodiffusion of alkali halide solutions in silica nanopores. *Nanoscale* **2020**, *12*, 23626–23635.

(53) Thomas, A. S.; Elcock, A. H. Molecular Dynamics Simulations of Hydrophobic Associations in Aqueous Salt Solutions Indicate a Connection between Water Hydrogen Bonding and the Hofmeister Effect. *Journal of the American Chemical Society* **2007**, *129*, 14887–14898, PMID: 17994735.

(54) Sun, C.; Zhou, R.; Zhao, Z.; Bai, B. Unveiling the hydroxyl-dependent viscosity of water in graphene oxide nanochannels via molecular dynamics simulations. *Chemical Physics Letters* **2021**, *778*, 138808.

(55) Abal, J. P. K.; Dillenburg, R. F.; Köhler, M. H.; Barbosa, M. C. Molecular Dynamics Simulations of Water Anchored in Multilayered Nanoporous MoS2 Membranes: Implications for Desalination. *ACS Appl. Nano Mater.* **2021**, *4*, 10467–10476.

(56) Netz, P. A.; Dorfmüller, T. Computer Simulation Studies on the Polymer-Induced Modification of Water Properties in Polyacrylamide Hydrogels. *The Journal of Physical Chemistry B* **1998**, *102*, 4875–4886.

TOC Graphic

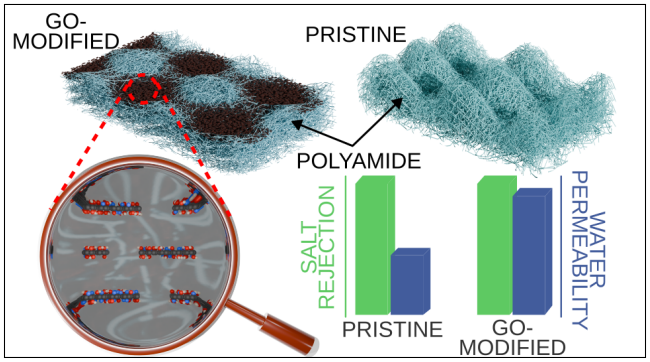
GO-
MODIFIED
PRISTINE
POLYAMIDE
SALT
REJECTION
WATER
PERMEABILITY
PRISTINE
GO-
MODIFIED